Viscous droplet in nonthermal plasma: Instability, fingering process, and droplet fragmentation

Lucia Potočňáková,* Petr Synek, and Tomáš Hoder†
Department of Physical Electronics, Masaryk University, Kotlářská 2, 61137 Brno, Czech Republic

(Received 4 September 2019; revised manuscript received 31 March 2020; accepted 7 May 2020; published 1 June 2020)

The interaction of dielectric barrier discharge plasma and silicone-oil liquid droplet in a Hele-Shaw cell was investigated experimentally employing synchronized optical and electrical time-resolved measurements. Temporal development of the destabilization, stretching, and fragmentation of the plasma-liquid interface was studied for the whole event lifespan. The perturbation wavelength and temporal development of fingering speed, plasma-liquid interface length, mean transferred charge, and fractal dimension of the pattern were determined. Recorded changes in the dissipated mean power show a strong correlation to subsequent stretching of the interface, opening new methodological possibilities for future investigations. Our extensive parametric study shows that oil viscosity and applied voltage amplitude both have a significant impact on the interface evolution. Notably, at relatively high voltages the destabilized interface featured properties noticeably diverging from the theoretical prediction of a known model. We propose an explanation based on the change of the liquid viscosity with increased heating at high applied voltage amplitudes.

DOI: 10.1103/PhysRevE.101.063201

I. INTRODUCTION

The interfacial instabilities, in general, are a complicated topic; the phenomena often observed experimentally but less frequently explained theoretically in a comprehensive way. The list of various instabilities in the field of plasma physics is rather extensive, let us name, for example, sausage instability, hose instability or filamentation as few of the more common ones. In the field of fluid dynamics, the well-known examples can be, e.g., Rayleigh-Taylor instability [1–3], requiring the interface between two fluids of different densities, Kevin-Helmholtz instability [4,5], happening at the interface with velocity difference between two fluids, or Saffman-Taylor instability [6–8], observed at interfaces of fluids with various viscosities.

Electrical forces can cause other types of instabilities in fluid interfaces. Various effects of electric fields and charge build-up in liquids have been known and studied for decades now [9,10]. The conversion of electrical energy to kinetic energy manifests itself in processes such as electrokinesis, electroosmosis or electrophoresis. Electrospinning [11] and electrospraying [12] techniques rely on electricity-induced deformation and dispersion of liquids. Radial electric field significantly affects the dynamics of viscous filament surrounded by another viscous fluid [13]. The charged toroidal droplets can even develop fingerlike structures; imposed electric stress determines the expansion speed of the torus, and its interface is destabilized [14].

The whole situation gets even more complicated when the present electric field is used to generate an electrical discharge plasma. Electric fields, charge generation and transfer, heating, gas composition and other dependent parameters are all directly affected by plasma presence. Moreover, plasma can get in direct contact with liquid; it can change the surface properties of the liquid and also of the surface of the experimental cell itself. The heated liquid changes its viscosity while the liquid electrification changes the surface tension at the same time. In turn, the properties of the plasma are also influenced by the proximity of other substances. The resulting system is quite intricate, and plasma-liquid interactions are becoming an increasingly important topic in the field of plasma science and technology [15–18]. While the breakdown phenomena in liquids [19], plasma-initiated chemistry [20], and its applications [21] are investigated frequently, the reports studying the stability of the plasma-liquid interface are rather scarce [22–25].

In this article, we study the liquid interface destabilization, stretching and fragmentation by nonthermal plasma. We investigate the viscous droplet interaction with atmospheric pressure plasma generated by the barrier discharge in a Hele-Shaw cell. We utilize a similar system as in Ref. [26] and consider it as a well prepared experimental model enabling further analysis of the phenomena on plasma-liquid interface and its investigation under a broader interval of initial conditions and scales. We follow the pioneering work of Chu and Hou *et al.* [25,26] and newly explore the crucial influence of a higher applied voltage and, using a novel methodology, we analyze detailed temporal development of electrical and optical recordings over the complete lifespan of the investigated event for the first time.

This paper also pays attention to discharge without the droplet and to the contraction of the cell due to the electrostatic force at the very beginning. We evaluate the synchronized temporal development of the main parameters, such as the speed of the fingering, interface stretching, fractal dimension of the generated pattern and the generated

*nanai@mail.muni.cz
†hoder@physics.muni.cz

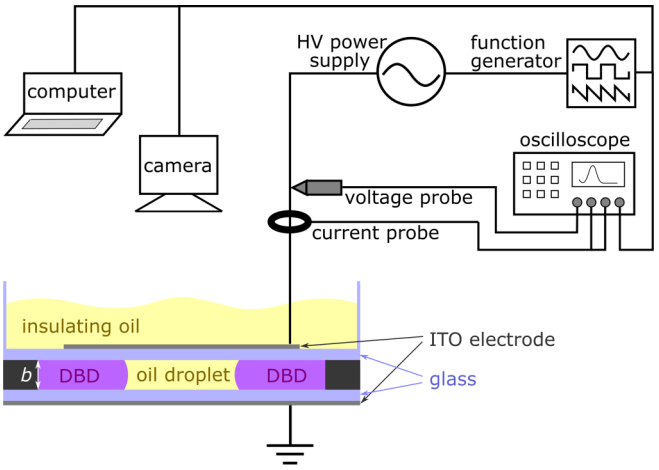

FIG. 1. The simplified schematic of the experimental setup for generation of the plasma in Hele-Shaw cell and its electrical and optical diagnostics. DBD denotes the dielectric barrier discharge plasma occurrence.

electrical charge, which is a measure of the dissipated energy in the system (see the description further in the text). In the final stage of the droplet fragmentation, i.e., when secondary droplets are generated as a result of complete fragmentation of the primary droplet, we analyze also the properties of these remaining secondary droplets. Above mentioned parameters are evaluated for different primary droplet volumes, viscosities, and applied voltages. Based on our extensive parametric investigations and analyses of obtained results, we are able to track in time the plasma events responsible for the interface stretching. We also propose an additional effect accountable for the fingering pattern at higher voltages which was not taken into account in previous investigations.

The paper is structured in the following way. In the next two sections, we describe the experimental setup and methods used during the processing of experimental data. The results section starts with the characterization of the dielectric barrier discharge plasma without oil droplet and only then the general behavior of the oil droplet in the plasma is reported. Further, various ways of the fingering process quantification are analyzed. Moreover, a detailed parametric study of the phenomena is done, exploiting the previously described techniques and presenting the novel results. In the last part of the results section, we analyze the phenomena theoretically.

II. EXPERIMENTAL SETUP

The schematic image of the experimental setup is shown in Fig. 1. The main part of the setup is the dielectric barrier discharge (DBD), depicted in color in lower part of Fig. 1. DBD plasma was generated between two glass sheets ($40 \times 40 \times 0.4$ mm), both serving as dielectric barriers, with thin layers of indium tin oxide (ITO) (320 nm) deposited on outer sides of them, acting as transparent electrodes (resistance approximately 30 ohm/sq). The glass sheets were separated by nonconductive spacers of variable thickness (0.05–0.16 mm), creating a gap of width b in which the plasma could be operated. In this thin gap between the glasses, the droplet of polydimethylsiloxane oil (density $\rho = 970$ kg/m^3, various kinematic viscosities $\nu = 50$, 100, 200, 350, and 500 mm^2/s, surface tension ranging for various viscosities only slightly from $\sigma = 20.7$ mN/m for 50 mm^2/s oil to $\sigma = 21.1$ mN/m for 500 mm^2/s oil, all at 298 K) was placed. The droplet was surrounded by ambient air. The glass sheets with the droplet in between form a Hele-Shaw setup.

The discharge was powered by ac high-voltage generator providing sinusoidal voltage operating at resonant frequency 12.5 kHz, with maximum voltage amplitude $U_{amp} = 10$ kV (20 kV$_{pp}$). Electrical measurements were performed with a voltage probe (Tektronix P6015A) and current probe (Tektronix CT-2) both connected to a high-resolution and high-sampling rate oscilloscope (Keysight DSO-S 204A 2-GHz 20 GSa). Imaging of the discharge was performed with an intensified charge-coupled device (ICCD) camera (PI-MAX3 1024RB-25-FG-43) equipped with a standard objective lens mounted above the discharge. The DBD system was observed by looking through the transparent top electrode. The ICCD camera and oscilloscope measurements were both synchronized with the discharge using a rectangular envelope. It resulted in a recording of the single-shot ICCD image and oscilloscope data during each segment. Additionally to this synchronized, but only grayscale video, a nonsynchronized digital camera (Nikon D7100) was used to capture color video with 24 frames/s for better illustration of the plasma and the process from its very start.

The procedure of each experiment was the following: the oil droplet of specified volume and viscosity was placed on the bottom glass. The spacers of the desired width were put in place, and an upper glass with an electrode was added from above. It squashed the droplet so that the droplet wetted surfaces of both the bottom and upper glasses. Shortly after, the sinusoidal voltage was turned on directly to the pre-set high amplitude value. The experiments were performed in a laboratory with room temperature kept constant at around 298 K.

III. DATA PROCESSING

The raw measured data from voltage and current probes were further processed by the custom-written script using NumPy [27] Python library. The time step between individual snapshots of the current and voltage waveforms was 140 ms. To suppress the stochasticity of each period, 130 periods, each of length $T = 80$ μs, were recorded each time and their average was used for further calculations.

The first parameter of interest was the applied voltage amplitude. Before the experiments, the discharge circuit was tuned into resonance. At the same time, the voltage amplitude was much lower than the breakdown voltage (e.g., 1 kV). When the discharge was ignited, the voltage started to drop as the capacity of the reactor changed. As a result, the system has moved slightly out of resonance. This change could be up to almost 1 kV (an example of voltage amplitude evolution can be seen in Fig. 4).

The crucial electrical parameter was the input reactor power P, which was calculated as integral of voltage U and

the current I over the averaged period:

$$P = \frac{1}{T}\oint UI\,dt. \tag{1}$$

However, as the voltage dropped, this parameter was also steadily decreasing, thus not providing desired insight. What was needed to know was the power per unit of the effective voltage in a measured time interval of τ. Not surprisingly, this variable has a dimension of the charge; namely, it is the absolute value of the charge transferred during the interval of τ. It can be understood as an averaged generation and transfer of free charges, e.g., electrons, which are in nonthermal plasma responsible for further rotational and vibrational excitation of the surrounding molecular gas and, consequently, its heating via energy depletion of these internal excited states to other heavy particle translation energy by mutual collisions. For brevity, we will address this as mean transferred charge or simply the charge throughout the paper:

$$|Q| = \tau\frac{\frac{1}{T}\oint UI\,dt}{\sqrt{\frac{1}{T}\oint U^2\,dt}}. \tag{2}$$

We can write this more simply in form of

$$|Q| = \frac{\tau P}{U_{\text{eff}}}, \tag{3}$$

where U_{eff} is the effective voltage defined for sine voltage waveform as

$$U_{\text{eff}} = \frac{U_{\text{amp}}}{\sqrt{2}}. \tag{4}$$

To process the ICCD camera video, another script was written using OpenCV [28] and NumPy [27] Python libraries. The main goal was to determine the shape of the unstable plasma-liquid interface and its length. The automatic processing was based on the fact, that plasma was glowing, while the area filled with oil remained dark. A Gaussian filter was applied to suppress the noise, and the edges of the image were detected by customized Canny edge detection algorithm [29]. However, the rather low luminosity of the plasma and sometimes extremely thin channels of oil created by extensive fingering in latter times of the oil droplet development resulted in rather low contrast in the images. As a result, data processing became problematic, and in some cases, not entirely reliable. Luckily, these cases can easily be distinguished and accounted for during the interpretation of the results.

IV. RESULTS AND DISCUSSIONS

A. Plasma without droplet

First, let us have a look at the plasma of our dielectric barrier discharge without the presence of the oil droplet. Figure 2 shows the main types of plasma appearance without the oil droplet. Each image was cropped from a larger frame to show only the region of interest inside the circular metal contacting of the ITO electrode, i.e., the area where oil droplet would be placed later. From Fig. 2, it is evident that plasma appearance can vary dramatically. Moreover, these changes can be triggered by only slight variations in operational conditions and, in rare cases, even seemingly spontaneously.

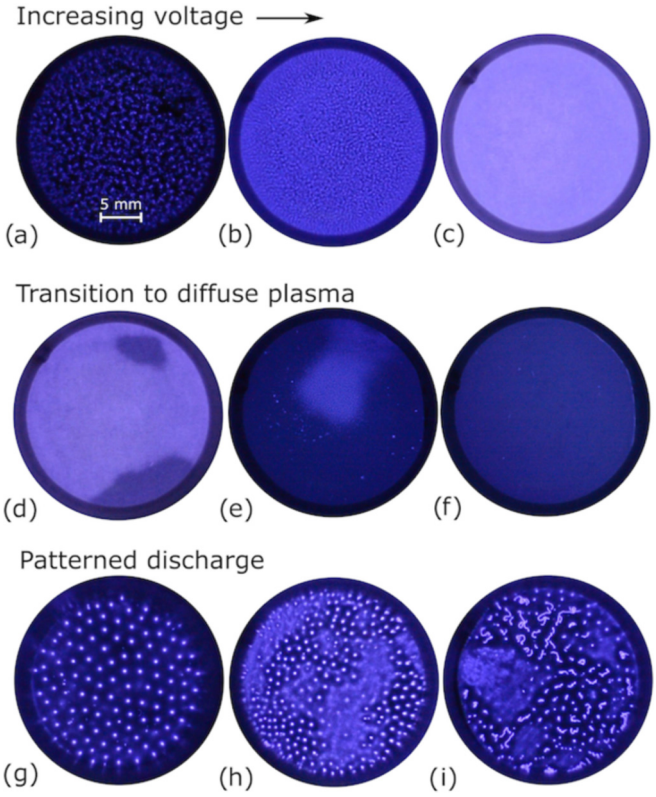

FIG. 2. The examples of plasma appearance in our experiment without the presence of oil droplet. [(a)–(c)] The filamentary plasma with increasing voltage, [(d)–(f)] transition to diffuse plasma, and [(g)–(i)] patterned discharge.

Figures 2(a)–2(c) represent the evolution of plasma with increasing voltage. Image (a) shows the discharge with the voltage only slightly above the ignition voltage with filamentary plasma not able to cover the whole interelectrode area. It operates in the form of isolated microdischarges, which are rapidly changing their positions. As the voltage is increased, the number of filamentary microdischarges increases as well [Fig. 2(b)], until they fully cover the observed area [Fig. 2(c)] and give a smooth homogeneous appearance. Plasma appearance in image [Fig. 2(c)] is also the case that was always desirable for the latter experiments with oil droplets. Figures 2(d)–2(f) represents the transition from homogeneous filamentary plasma to a diffuse plasma. Other than optically, this transition could also be noticed from the discharge current measurements. In filamentary mode, the discharge current waveform consisted of many short current spikes corresponding to individual microdischarges. In the diffuse regime, there was only one breakdown peak visible, followed by broad flat hump, as also evidenced by many other authors [30–33]. Such transition often occurred spontaneously after some time, possibly triggered be electrode heating. Typically it started from outside and spread toward inside. The two types of plasma could coexist [Figures 2(d)–2(e)] several seconds with their interface slowly and fluently moving, until the system reached stability with either the full coverage by diffuse [Fig. 2(f)] or filamentary [Fig. 2(c)] plasma.

Figures 2(g)–2(i) show the patterned discharge [34,35], which was the third distinctive kind of plasma that was observed in our experiments. In such case, the individual filamentary microdischarges did not cover the whole area; however, in contrast to image (a), the filaments, in this case, were very bright and quite thick. The filaments could be arranged in a stationary pattern with no movement at all [Fig. 2(g)], slowly changing pattern [Fig. 2(h)] or with the microdischarges moving rapidly at short distances but maintaining the overall pattern relatively stable [Fig. 2(i)]. The coexistence of patterned discharge with homogeneously looking discharge [Figs. 2(h) and 2(i)] was more probable than purely patterned discharge [Fig. 2(g)].

B. Liquid droplet in plasma

The experiments with the oil droplet were always performed under such conditions, that would in the absence of the oil droplet have resulted in the plasma appearance as depicted in the first row in Fig. 2. Preferably with the voltage high enough for plasma to homogeneously cover the whole discharge space [Fig. 2(c)]. However, the presence of the droplet itself could sometimes affect the plasma appearance, as will be shown later. Possible reasons for this could be smaller discharge area (by the area of the droplet) or the contamination of the discharge space with oil vapor. The local thinning of the gas gap due to the layer of the residual oil remaining on the glass surfaces after the droplet pass-over could play a role as well.

1. Instability and fingering process

The experiments with droplet were performed for a wide range of experimental conditions. The controlled variables were the voltage, the gap width, the viscosity of the oil and the oil droplet volume. Although various combinations of these parameters led to different experimental results (as it will be detailed later), the generalized description of the droplet behavior similar to some extent for most cases can be found and is shown in a sequence of video frames in Fig. 3. There, one can recognize the initially stable squashed droplet in the Hele-Shaw cell as a dark circle in the center, surrounded by the lighter violet coloured air plasma of the DBD. With increasing time, the plasma-liquid interface destabilizes, and the fingering process is initiated—plasmatic fingers intrude the droplet. After several seconds the liquid between the plasmatic fingers is stretched beyond a certain threshold, and the fragmentation starts. Finally, the event finishes with complete fragmentation of the original droplet into the many secondary droplets.

In Fig. 4, the first 6 s of another such process are quantified using the following time-dependent parameters. These are the droplet area, the inner and outer radius of the droplet, the finger length (i.e., the difference between the two radii) [all Fig. 4(b)], the plasma-liquid interface length, the fractal dimension of the generated pattern [both Fig. 4(c)] and the electrical parameters of dissipated power and its measure weighted by the voltage, i.e., the mean transferred charge [both Fig. 4(d)]. The droplet area was analyzed based on binarization of the images via advanced multistep thresholding. The inner and outer radii of the unstable interface

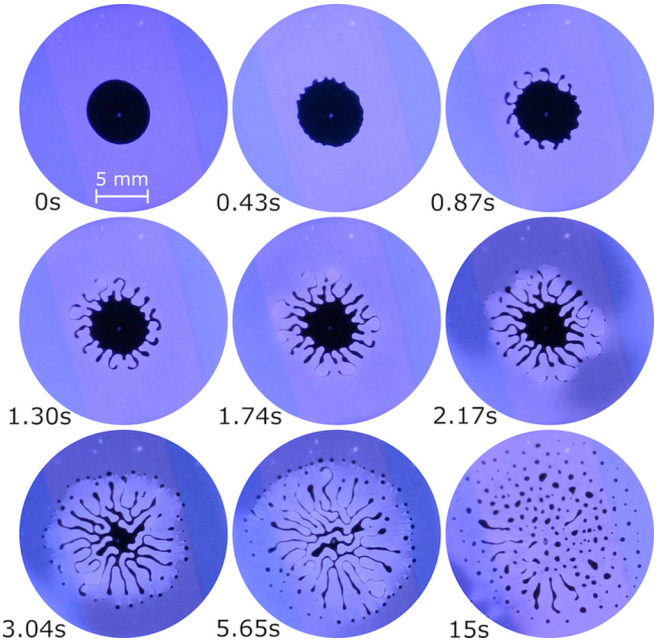

FIG. 3. An exemplary evolution of the oil droplet affected by plasma, from the moment of plasma ignition until the total fragmentation of the main droplet into secondary droplets. Please note that the frames are not evenly time spaced but manually selected to best illustrate the whole process. The corresponding video of the process can also be seen in the Supplemental Material [36]. Experimental conditions: droplet volume $V = 4\ \mu$l, viscosity $\nu = 100\ \text{mm}^2/\text{s}$, voltage amplitude $U_{\text{amp}} = 5.8$ kV, and gap width $b = 0.1$ mm.

were evaluated according to the schemes shown in Figs. 5(a) and 5(b), where the resulting finger length is depicted as well. The length was increasing linearly which enabled also the determination of the speed. The interface length was determined using a Canny edge detection [29]. The measure of plasma penetration into droplet is also reflected in the complexity of the resulting areal pattern, which resembles a fractal behavior. The fractal dimension of the droplet area pattern was determined by box-counting method [37]. Each data point in the graphs in Fig. 4 corresponds to one video frame of the droplet fragmentation for which analyses mentioned above were performed.

When the voltage is applied to the prepared system, the filamentary plasma homogeneously fills the discharge area almost instantly. It happens in order of ones to tens of milliseconds, which is negligible compared to the timescale of observed phenomena from hundreds of milliseconds to tens of seconds. Right afterward, the droplet's surface slightly widens, due to the electrostatic attraction of the glasses squashing the droplet even more. This is shown in Fig. 4(b) as the changes in the droplet area. At this very beginning (zeroth phase) there are no fingers yet, i.e., only one radius of the droplet is measured and it increases; in the graph, it is plotted as the inner radius. The attraction also continues after the fingering instability has begun in the first phase, until the peaking value of the dissipated power [and of the transferred charge, see Eqs. (1) and (3)]. This attraction was not the cause of the instability, certainly not in the sense of pressure-driven viscous fingering, as the squashing of the cell leads to pushing

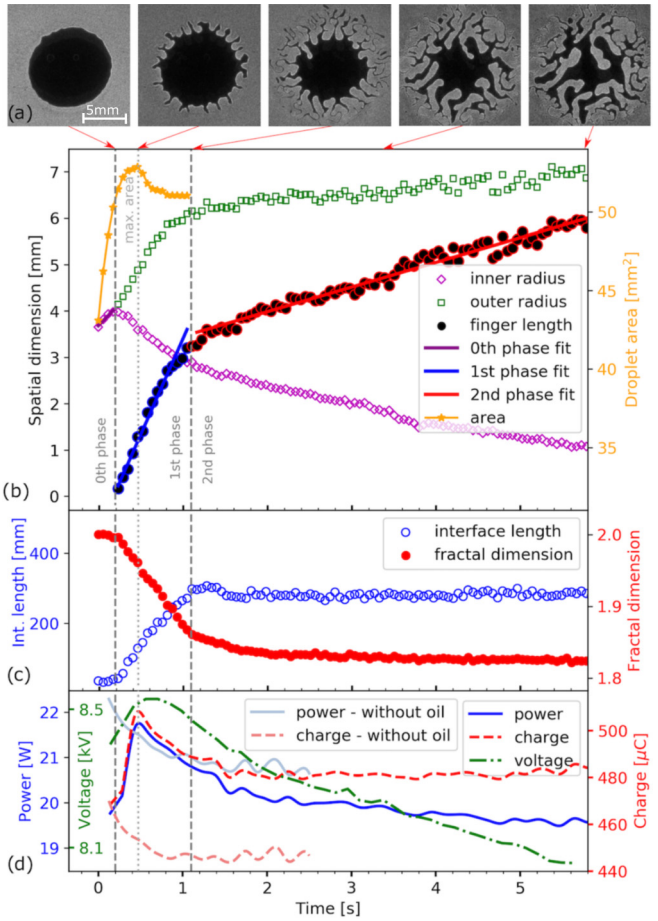

FIG. 4. Time development of the typical fingering process event, imaging in part (a). The area of the oil droplet, its inner and outer radii (b), interface length and fractal dimension (c), and electrical parameters (d) are shown. The frames (a) correspond to data points in times marked by red arrows, i.e., at 0.2, 0.45, 1.1, 3.4 and 5.8 s. Experimental conditions: droplet volume $V = 8\ \mu$l, viscosity $\nu = 100\ \text{mm}^2/\text{s}$, voltage $U_{\text{amp}} = 8.4$ kV, and gap width $b = 0.1$ mm.

the high-viscosity oil toward the surrounding low-viscosity air plasma. While for the Saffman-Taylor instability to arise, it needs to be the other way around—lower viscosity liquid pushing toward higher viscosity one. The speed of enlarging of the squashed droplet in the zeroth phase [i.e., expanding of the droplet radius, denoted as a magenta linear fit in Fig. 4(b)] is 1.88 mm/s.

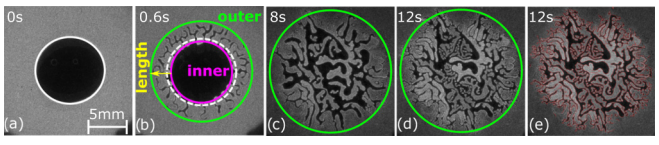

FIG. 5. The finger length was evaluated as a difference between the mean inner and outer radii, see parts (a) and (b). The ICCD camera frames of the droplet in advanced state of fingering process are shown in parts (c), (d), and (e). The interface between plasma and oil regions, as detected by Canny edge detection, are retraced in red in (e). Experimental conditions: droplet volume $V = 8\ \mu$l, viscosity $\nu = 100\ \text{mm}^2/\text{s}$, voltage $U_{\text{amp}} = 10$ kV, and gap width $b = 0.1$ mm.

Based on these observations, we can hypothesize that the electrostatic attraction of the glass electrodes and subsequent microscopic squashing of the oil in the cell is the reason for the change of the droplet area in the experiment presented by Chu *et al.* [25], i.e., the shrinking of the plasma bubble in the inverse plasma-liquid set-up. Also, the results show that the droplet area reaches its maxima at the moment of peaking charge shortly before the peaking applied voltage [as shown for the event in Fig. 4(d)]. It is consistent with the fact that within the gap, the local electric field or voltage (so-called gap voltage, see Refs. [30,38,39]) responsible for the cell squashing does not correspond to the applied voltage amplitude in the external circuit. The applied voltage is not the suitable parameter to asses the electrical effects in the gap due to the residual surface charge and capacitive coupling of the dielectrics. We intend to deal with this finding in our future work.

The plasma-droplet interface destabilization starts approximately 0.2 s after plasma ignition (the first phase of the fingering process is initiated, see Fig. 4). The interface is warped by the seeds of plasmatic fingers, which then continue to expand into the interior of the oil droplet. This is similar to the viscous fingering process when fingers of less viscous liquid penetrate the more viscous one. The primary destabilization and fingering of the plasma and the droplet is rather abrupt and lasts another 1–2 s (approximately 1 s in the case presented in Fig. 4), during which all parts of the droplet remain connected. At this primary phase of the droplet evolution, a certain level of regularity in the droplet shape is still present even though the neighboring fingers are already starting to compete for space and branch. The fingers of plasma grow inward the droplet, which means that the competition for space is the dominant process, and the fingers' growth inward is limited by the size of the droplet. The receding channels of the oil pushed out by the plasma intrusion are moving in the opposite direction, and they contribute to the plasma fingers effective length. Figs. 5(a) and 5(b) show how all this was considered when discussing the prolongation of plasma fingering in our experiments. The difference between radii of circles fitting the tips of plasma fingers (the inner circle) and their bases (or the tips of receding oil threads, i.e., the outer circle) was used to determine the average fingers' length. The temporal change of this length, of the finger prolongation, is in each phase linear and considered the speed of fingers' growth for that phase. This speed (or prolongation rate) of the fingering in the first phase was quantified for the case in Fig. 4 to be 4.13 mm/s [blue fit of the black circles in the first phase plot area in Fig. 4(b)].

For the event studied in Fig. 4, there is a clear change in the fingering speed at 1.1 s. Suddenly, the rate of the change of the fingers' length decreases. We describe this moment as the start of the second phase. The higher speed of the first phase, compared to the slower second phase, may be explained by the fact that at the beginning of the fingering the channels of oil were relatively wide and short and it was easy for plasma to push out more oil through them outward to the periphery. The second phase is in general slower [0.51 mm/s, denoted as a red linear fit of the black circles in the second phase plot area in Fig. 4(b)], as the system is evolving toward equilibrium and the oil channels are thinner and longer. The parametric study

of the fingering speed is presented later in the text and showed in Fig. 14.

The temporal development of the interface length can be followed in Fig. 4(c). Within the first phase (time interval of approximately 1.1 s) the interface stretches by one order of magnitude, from approximately 30 to 300 mm. In the second phase of the event presented in Fig. 4, the interface does not seem to stretch anymore, and the length remains almost stable. Nevertheless, this is not always the case. Figures 5(c) and 5(d) show another droplet in the late second phase for higher applied voltage than in the event described in Fig. 4. Even though the time difference between the two frames is 4 s, in both frames the inner radius would be zero, as plasma fingers already penetrated the center of the droplet, and the outer radius is also the same for both cases. Yet, the plasma continues to fill up the inner spaces of the droplet and stretches the interface further by splitting into thinner plasmatic fingers. By detecting the outlines of the fingers [red in Fig. 5(e)] and measuring the length of the interface, are able to quantify the difference between images in Figs. 5(c) and 5(d). In this particular case the interface lengths are 423 and 663 mm. That is stretching rate of over 200 mm within the 4 s.

In general, the plasma effects cause that the pattern of initially well-rounded droplet becomes more complicated. In the later times of the development, the fingering process continues not symmetrically in relation to the center of the droplet as the fingers start to branch and fold, creating a fractal pattern. To describe this process quantitatively, we have evaluated the fractal dimension parameter using the box-counting method, see in Fig. 4(c). This parameter starts at the value of 2, as expected. Within the zeroth phase it does not change as the fingering has not started yet. During the first phase, however, the fractal dimension rapidly decreases to approximately 1.85. While the interface length remains constant in the second phase (becoming insensitive as a description parameter for the event shown in Fig. 4), the fractal dimension parameter appears to still be sensitive. It decreases toward the value of 1.82 after 5 s. That means that the generated pattern becomes more and more complex, yet not as a result of the interface stretching [in contrast to the event in Figs. 5(c) and 5(d)] but due to the interface folding and local contortions [40]. On a longer timescale, the value of the fractal dimension decreases further toward the value of approximately 1.8. However, the complexity of the pattern and the limited robustness of the evaluation procedure caused that the uncertainty of the obtained value of the fractal dimension could be up to ± 0.03.

Figure 4(d) shows the temporal evolution of discharge power, voltage and mean transferred charge. It was commented in Sec. III, that after the discharge ignition, the capacity of the reactor changes. As a result, the system gets out of the resonance, which results in observed changes in voltage amplitude (green dash-dotted line). The subsequently decreasing voltage also affects the measured reactor power (blue solid line). So the power per unit of the effective voltage was calculated, i.e., the mean transferred (or generated) charge within the gap (red dashed line)—for more details see again Sec. III. For comparison, also the experiment without droplet, i.e., only with undisturbed plasma is plotted here. It can be seen that the droplet presence influences both power and charge development. Except for the difference in the numerical values with or without droplet, the most prominent distinction between the two sets of curves is the presence of the peak in the experiment with oil droplet and its absence without the droplet. We account this effect to the change of the characteristic capacitance of the setup due to the presence of the liquid droplet and changes in ionization and surface charging rates at the triple line of the plasma-liquid-dielectric surface contact.

In summary, the contrast between the first and second phase indicates different phenomena dominating the fingering process. The first phase has a short burstlike character defined by a rapid increase of the electrical parameters and ends when the droplet reaches some equilibrium. The mean electrical power and transferred charge both slowly relax in the second phase. As a result, its evolution is slow and gradual. With general equilibrium already instated, it is much more dependent on local conditions which can vary not only among the droplets but also among different parts of one droplet. The second phase also lasts much longer, and so all locally driven irregularities in the droplet motion get averaged to a surprisingly stable value, e.g., for the fingering speed parameter. The two-phase character is very well discernible on the evaluation of the interface length and fractal dimension parameters with a very sharp transition between these phases.

2. Secondary droplets

The plasma fingers intrude the droplet to its center, stretching all of the liquid to very thin fibres and folding them. Some of the outer ends of oil channels can be rapidly moving in a whiplike motion. As they are stretching longer, the tiny droplets can be expulsed from the main body of the liquid, which continue to be expelled further out. The fragmentation of the primary droplet continues until it is torn to tens of tiny droplets, which do not split any further but can continue to move in the Hele-Shaw cell.

The secondary droplets and their behavior can promote the understanding of fingering process of the main droplet. They represent the basic unit of the oil affected by plasma under given conditions. After their formation, the secondary droplets are too small to undergo further fingering themselves. Their diameter is smaller or comparable to the wavelength of perturbation, i.e., the primary droplet circumference divided by the number of plasmatic fingers for given conditions. Nevertheless, the discharge can manipulate them to change their positions. The conditions leading to movement of the secondary droplets usually involve the asymmetry in the discharge optical emission intensity and/or character (compare Figs. 3 and 6). It is worth noting that in the case without the oil droplet, the diffuse or filamentary nature of the discharge could be confirmed by electrical measurements. With the oil present however, the discharge is never fully diffuse (see Fig. 3) and optically less intensive areas are presumed diffuse based only on visual similarity.

If the plasma in the vicinity of the secondary droplets is homogeneous, either all more intensive (filamentary) or all less intensive (diffuse), then the droplets can form a fixed pattern. However, it is different for secondary droplets near the interface of the two regimes, where gradients in charge transfer (i.e., gradients in energy dissipation or charging) and

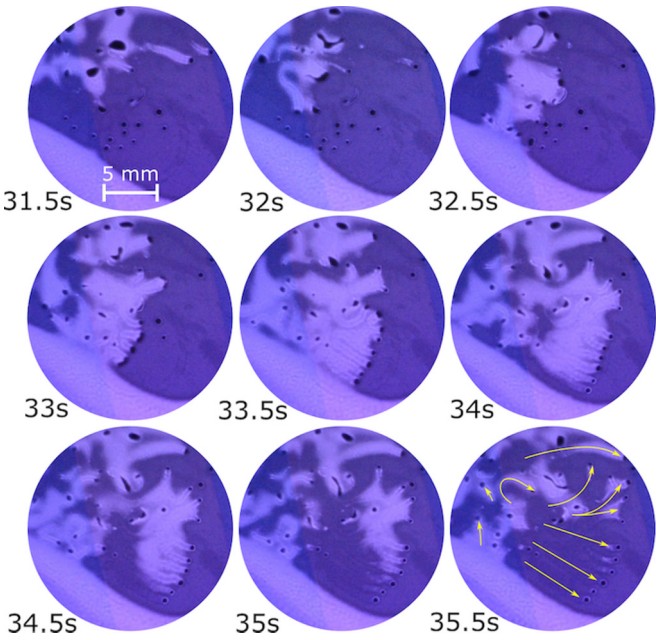

FIG. 6. The chainlike reaction of secondary oil droplets after the complete fragmentation of the main oil droplet. The paths of some noteworthy traveling droplets are highlighted by yellow in the last image. Experimental conditions: original droplet volume $V = 4\ \mu$l, viscosity $\nu = 100\ \text{mm}^2/\text{s}$, voltage $U_{\text{amp}} = 6$ kV, and gap width $b = 0.1$ mm.

temperature are expected to be the strongest. In such a case, the droplets can get out of their balance and be put in motion, with the direction of the oil flow from filamentary toward diffuse plasma region.

The filamentary and diffuse regions of plasma are visible in both Figs. 3 and Fig. 6 and their locations seem to be in relation to the droplet actions. In Fig. 3, initially filamentary discharge starts to be replaced by diffuse plasma from outward, in the regions undisturbed by the droplet. The central areas affected by the droplet, i.e., in close vicinity of the droplet or at oil's previous locations, remain filamentary. As the primary droplet enlarges its effective radius, filamentary plasma again reclaims the majority of the discharge area. The circle of secondary droplets is moving together with the circular interface between the two types of plasma until the almost whole discharge is filamentary again.

Figure 6 shows another example of secondary droplets after the complete fragmentation of the main droplet. The discharge, in this case, is less homogeneous than in Fig. 3, with the bright filamentary region in the lower part of images and predominantly diffuse area with secondary droplets located in the upper part. In this frame sequence, it is visible how the group of secondary droplets is being pushed forward to the right by intensive plasma region emanating from the left. The trail of intense plasma also remains in previous locations of the moving droplet but extinguishes shortly. In such manner, the moving secondary droplets being pushed away by filamentary plasma region and simultaneously creating filamentary region behind them can propagate into the proximity of other secondary droplets and interact with them in chainlike reaction.

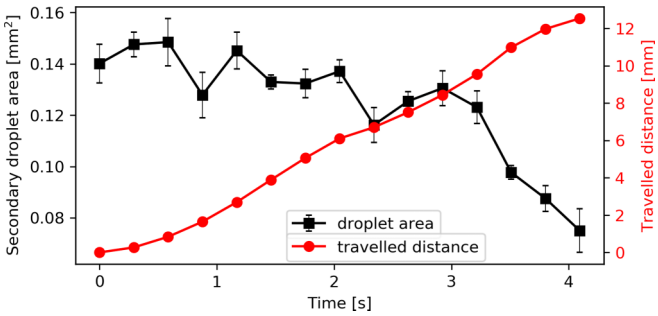

FIG. 7. The tracking of one secondary droplet as it travels through the discharge, being pushed by intensive plasma region and changes its size by losing or gaining oil to or from glass surfaces. Experimental conditions: original droplet volume $V = 8\ \mu$l, viscosity $\nu = 100\ \text{mm}^2/\text{s}$, voltage $U_{\text{amp}} = 5.5$ kV, and gap width $b = 0.1$ mm.

The filamentary-plasma-trail-generating moving secondary droplets can travel significant distances before the re-equilibration, as is shown in Fig. 7. Single secondary droplet has traveled the distance longer than 1 cm without any close interaction with another droplet, before finally stopping. Its area is generally decreasing, as the thin layer of oil from the droplet has been adhering to the glass surfaces. However, there have also been moments when the droplet area enlarges slightly, probably as it collects some oil after passing through the trail left behind some earlier secondary droplet. Although these trends are present, the uncertainty in measuring the area of such small droplet is high, as the secondary droplet size is near our resolution limit.

C. Parametric study

1. Oil droplet volume

As the droplet is squashed in the thin constant-thickness gap between the electrode glasses, the volume of the droplet sets the area of it. The exact droplet volume was set by micropipette, for this test in the range between 1 and 10 μl. In most of the other experiments however, it was kept constant at 8 μl (alternatively also 3 μl). There are several possibilities, how to quantify the start of the fingering process in the first phase or, in our case, the droplet behavior at the beginning of the destabilization of its interface [25,41,42]. To determine the characteristic wavelength λ of the initial perturbation is a way to describe the physical conditions ruling the primary droplet break up. Figure 8(a) shows one example of droplet few moments after plasma ignition with short fingers starting to spread. The number of fingers n was counted (small red circles in the figure), and with the knowledge of the droplet diameter d, their average wavelength λ is easily calculated as $\lambda = \pi d/n$.

The graph in Fig. 8(b) then shows interesting fact, similar as for the inverse problem (plasma bubble as reported in Ref. [25]), that even though the number of fingers increases for bigger droplets, their wavelength remains constant, if other conditions are fixed. It indicates (for both cases) that at the beginning of the droplet evolution, the driving forces act only on the interface and the bulk of the droplet does not affect the initial perturbation. The curvature radius also has no effect, at

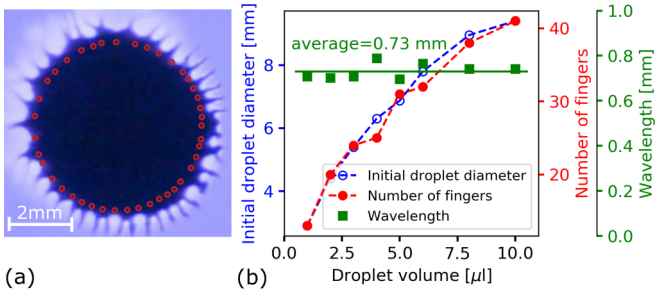

FIG. 8. The counting of the plasmatic fingers intruding the oil droplet just after their formation in order to calculate the wavelength of initial perturbation is shown in part (a). Experimental conditions: droplet volume $V = 4$ μl, viscosity $\nu = 100$ mm^2/s, voltage $U_{\text{amp}} = 9$ kV and gap width $b = 0.1$ mm. In part (b) the dependence of primary droplet diameter, number of the fingers and their wavelength for various oil droplet volumes are shown. Experimental conditions: viscosity $\nu = 100$ mm^2/s, voltage $U_{\text{amp}} = 6.3$ kV, and gap width $b = 0.14$ mm.

least in here examined range. The extreme case of the straight interface still maintaining the same perturbation wavelength as curved one was also demonstrated in Ref. [26]. However, if the droplet's initial size is comparably small or smaller than the wavelength of the perturbation, the fingering does not occur at all.

The overall process of the fingering is also very similar for small and big droplets. Figure 9 shows an increase in interface length in time during the whole fingering process [Fig. 9(a)] (in millimeters) and in detail for the first phase [Fig. 9(b)] (in relative scaling—the maximum and minimum for each trend are aligned to enable qualitative comparison). The rapid expansion of the droplet starts at the same time for every droplet size (approximately 0.3 s), the stabilization after the first phase takes place also after approximately the same time (0.8–0.9 s) and the transition between the phases is always pronounced and sharp. Thus the rate of interface length increase in absolute terms is higher for bigger droplet as it reaches much higher values at the same time. Nevertheless, scaling the plot relatively [see Fig. 9(b)] shows almost the same curve for each droplet volume.

Figure 9(c) shows the overview of the mean transferred charge development in time for various droplet volumes, i.e., the mean voltage-weighted dissipated power. With increasing volume of the droplet, the charge decreases. Larger droplet covers more of the interelectrode area with oil and blocks the discharge from being there, and thus overall charge decreases. The primary maximum charge is for given conditions (applied voltage and viscosity, i.e., the driving force and the liquid resistance, respectively) reached in approximately the same time for all different droplet volumes, similarly as the primary interface length maximum. (Please note that the interface length primary maxima for different droplet volumes have very different values ranging from 30 mm for 1 μl to 175 mm for 10 μl). The first phase is therefore finished at the same time (compare the Fig. 4) for all droplet volumes. This fact supports the results of the wavelength evaluation that the initial length of the interface does not affect the fingering process fundamentally and that the characteristic timescale of the phenomena in the first phase does not change for different droplet volumes, i.e., initial interface lengths.

2. *Oil viscosity*

In our experiments, five silicon oils with their kinematic viscosities ranging from 50 to 500 mm^2/s were used. Generally, with the change of viscosity, some other parameters of the oil can be affected as well. The mobility of the oil in Hele-Shaw cell strongly depends on viscosity; is defined as $M = b^2/12\nu$, where b is the gap width, and ν is the kinematic viscosity of the oil. The surface tension of the used silicon oils is almost stable for various viscosities, at 298 K ranging only between 20.7 and 21.1 mN/m and such minor changes are supposed to be insignificant in this experiment. Dielectric properties and heat conductivity are, in examined range of viscosities, almost constant as well.

However, the viscosity itself is strongly dependent on the oil temperature. In temperature range between 223 K to 523 K, the oil viscosity varies exponentially. The temperature of the oil was not directly measured in our experiment but can roughly be estimated based on general information about the discharge and its power consumption (see, e.g., Ref. [39]). Expectedly, the oil could get heated up by tens of degrees and the outer layer of the oil in direct contact with plasma even more, which would have a considerable effect on the experiment due to viscosity and surface tension decrease. We

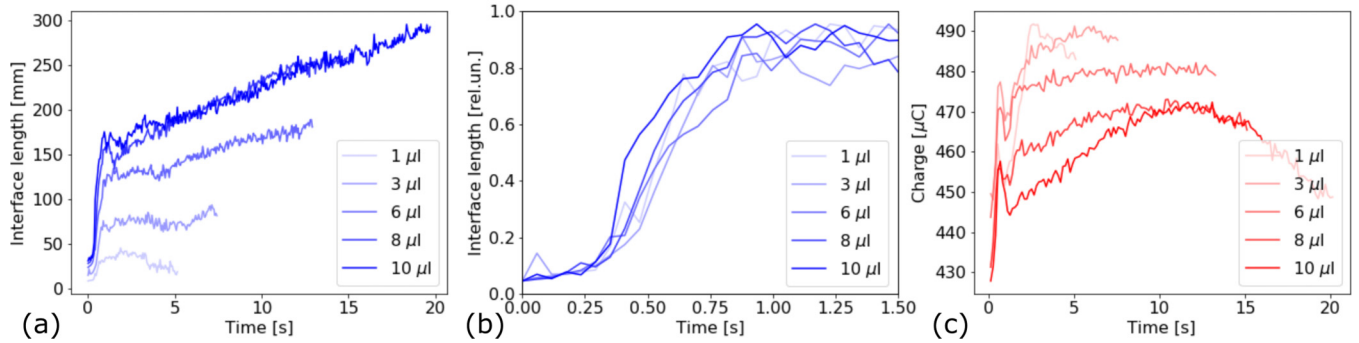

FIG. 9. (a) The interface length during the whole fingering process and (b) in detail for the first phase (please note the relative scaling) and (c) mean transferred charge during the whole fingering process with droplets of various volume. Other parameters were kept constant at viscosity $\nu = 100$ mm^2/s, gap width $b = 0.1$ mm, and voltage $U_{\text{amp}} = 7.7$ kV.

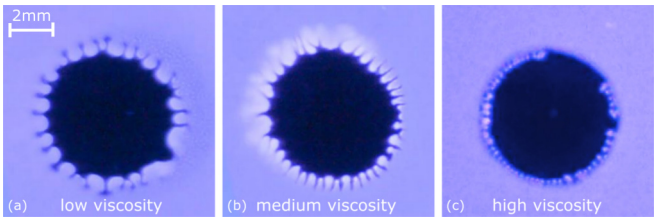

FIG. 10. The early phase of fingering in droplets of various viscosity oils. Experimental conditions: droplet volume $V = 4\ \mu$l, voltage $U_{amp} = 9$ kV, gap width $b = 0.1$ mm, (a) low viscosity $\nu = 50$ mm^2/s, (b) medium viscosity $\nu = 100$ mm^2/s, and (c) high viscosity $\nu = 350$ mm^2/s.

analyze this effect in more detail in the theoretical section (Sec. V) of this article.

The viscous fingering is affected by viscosity mainly through the changes in fluid mobility. It influences the wavelength and shape of plasma fingers and oil regions between them (see Fig. 10) as well as fingering speed. Using lower viscosity oil, i.e., the more mobile one, leads to fewer wider fingers separated by thicker oil channels, i.e., longer wavelength of the interface perturbation. Qualitatively the same result was also observed in Ref. [26]. Based on our parametric study of temporal changes of the interface length we can add that for higher viscosity the fingering generally starts few moments (tenths of a second) later after the voltage switch-on than in low viscosity [visible in Fig. 11(b)]. A possible reason for this is that the mobility of high viscosity oil is too low for the fingering to begin until the oil in contact with plasma heats up. Nevertheless, the changes in the timing are minimal [see Fig. 11(b)] and the variation interval in the overall development of interface length for different viscosities is rather tight. After the plasma fingers entered the heated outermost layer of the droplet, their advance slows down or ceases altogether. The unheated low mobility center of the droplet remains undisturbed by the perturbation of the interface, and the limited propagation of the plasmatic fingers inward causes also heating of only a limited interface length, cumulatively slowing down the fingering process. The second phase of fingering is hence almost a stable state for high viscosity oils, with minor or no movement at all (for the highest viscosity oil the fingers sometimes even retracted). The cease of further fingering is reflected in Fig. 11(a) as a constant (or even slightly decreasing) value of interface length for high viscosity oil. For the low viscosity oil, the fingers quickly and continuously penetrate to the center of the droplet and the transition between the phases 1 and 2 is more fluent [see Fig. 11(a)].

In terms of total values of the interface length, events with lower viscosity oil yields longer interface. Even though the number of fingers is lower, and they are thicker, it is compensated by their length (more significant prolongation than in high-viscosity oil) and by continued stretching in the second phase. As for the charge, there is no explicit dependence on viscosity [see Fig. 11(c)]. Comparing the values of the voltage-weighted mean dissipated power, one can see that similar amount of power is consumed for experiments with different viscosities (expectedly, as the U_{amp} is the same).

3. Voltage

Voltage is a specific parameter in that it primarily affects the plasma rather than the droplet. Yet, via more intensive heating for higher voltages (compare Ref. [39]), the local viscosity of the droplet is finally manipulated as well. The study of tendencies for various voltages was performed mostly in low viscosity oil, as it has proven to be more responsive to discharge changes. The voltage ranged approximately from 4 to 10 kV in amplitude (i.e., 8 to 20 kV$_{pp}$). The upper limit is set by insulating limitation of the experimental setup and lower limit by the fingering appearance condition itself. With decreasing voltage, the number of fingers decreases as well while their wavelength increases. For voltages too low, the plasmatic fingers are not able to protrude the droplet in a repeatable manner. Instead, the droplet just deforms and sways slowly in irregular shapes (see Fig. 12).

Figure 13 shows the interface length and mean transferred charge in the cell, both during the whole fingering process (in proper scale) and in detail for the first phase only (in relative scaling to the amplitude). It shows that the interface length starts to increase sooner for higher voltage; the increase is also sharper and reaches higher values than in low voltage experiments. Moreover, the transition between phases is more pronounced, the stretching in the second phase is more extensive, and the first phase duration is shorter than for lower voltage events. Some of these conclusions are well

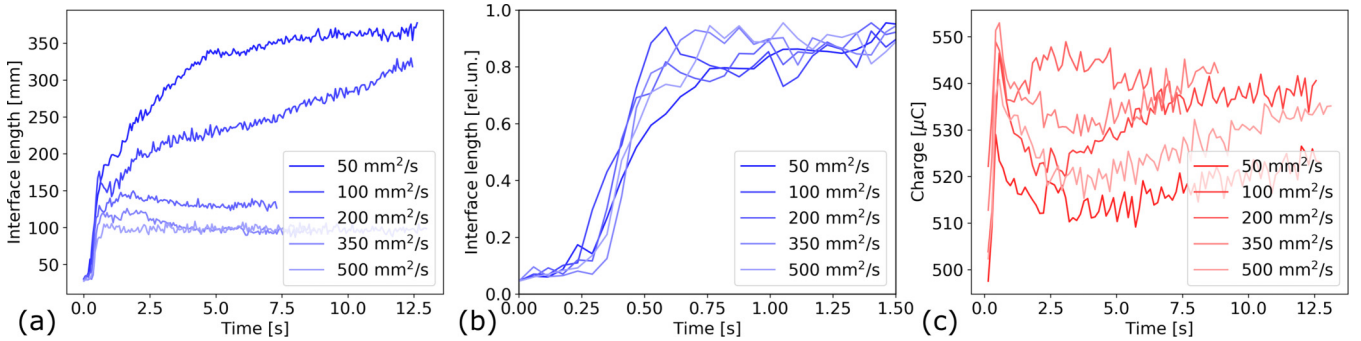

FIG. 11. (a) The interface length during the whole fingering process and (b) in detail for the first phase (please note the relative scaling) and (c) mean transferred charge during the whole fingering process with droplets of various viscosities. Other parameters were kept constant at droplet volume $V = 8\ \mu$l, gap width $b = 0.1$ mm, and $U_{amp} = 9.5$ kV.

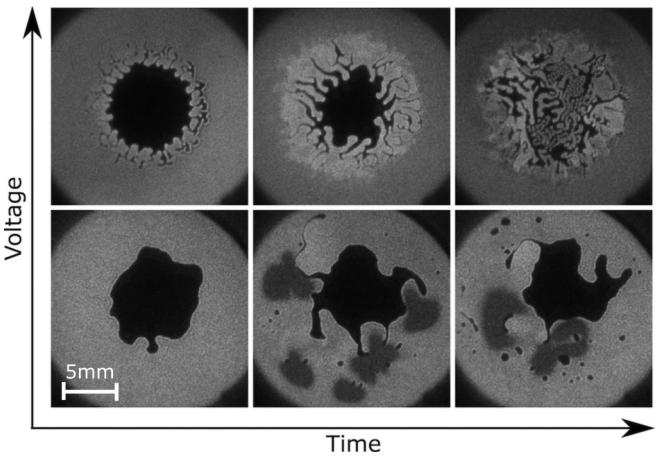

FIG. 12. The typical process of fingering driven by low and high voltage. Experimental conditions: droplet volume $V = 8\ \mu$l, viscosity $\nu = 100\ \text{mm}^2/\text{s}$, gap width $b = 0.1$ mm, lower voltage $U_{\text{amp}} = 4.3$ kV, and higher voltage $U_{\text{amp}} = 10$ kV.

visible in Fig. 13(b) thanks to the relative scaling, where the minimum and maximum values of each trend are at the extremes of vertical range. Apparently, in comparison with the previous two parameters, the voltage amplitude is the dominant parameter, significantly affecting the characteristic timescales and amplitudes of the fingering phenomena. This fact is even more visible for the evaluation of the transferred charge dependency. Figure 13(c) reveals that charge increments in steps with applied voltage amplitude; this is clarified by increased discharge filaments density. The most notable feature in its trend is the peak at the beginning, temporally corresponding to the first phase of the fingering. In the detailed plot in Fig. 13(d), the charge waveforms are shifted to the same baseline so that the steplike increments are discarded. Yet, the peaks' heights of the individual trends are unaffected and directly comparable. Additionally, the peaks maxima are highlighted by grayscale dots for easier readability. It is apparent that this peak maximum shifts to higher values and earlier times with increasing voltage, just as was the case for the interface length in the first phase in Fig. 13(b). The transition between the first and the second phases is, therefore, strongly manipulated by the voltage amplitude.

The above discussed is also apparent from the Fig. 14, where the applied voltage amplitude dependency of the characteristic fingering speeds for different fingering phases is shown, including the speed of the droplet squashing in the zeroth phase. It is shown for two primary droplet volumes. The droplet volume does not affect these speeds much—the speed of expansion seems to be generally lower for smaller droplets, but no reliable conclusions can be drawn, as the measured difference in speeds falls within the measurement error. Clearly, the fingering speed of the first phase is strongly, and linearly (compare with Ref. [26]), dependent on the applied voltage amplitude and, as mentioned earlier, it is the highest characteristic speed evaluated in comparison with speeds of other phases. The zeroth phase speed of droplet squashing shows not so profound yet detectable dependency on the voltage amplitude as well, confirming the hypotheses that the electrostatic squashing of the droplet is responsible for its growing area in the zeroth phase as described earlier. In Fig. 14(b), the fingering speed in the second phase only is

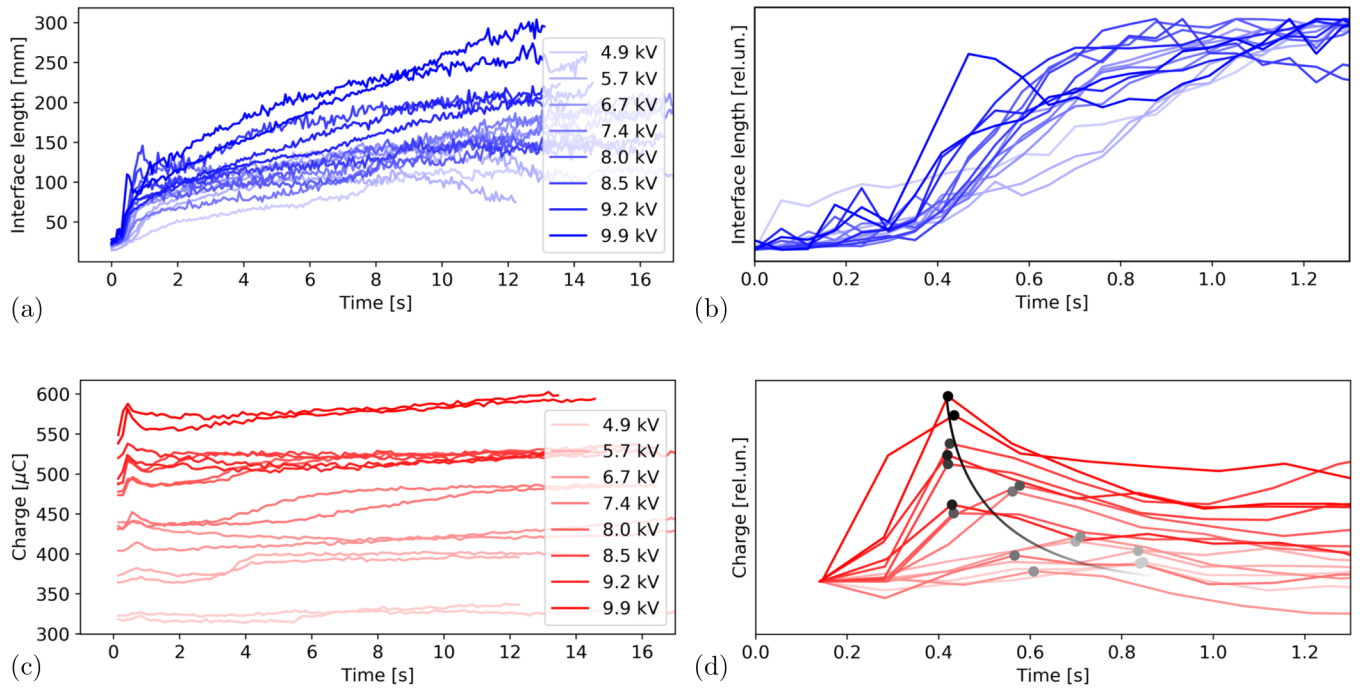

FIG. 13. (a) The interface length [detail of the first phase with relative scaling in (b)] and (c) mean transferred charge [detail of the first phase with relative scaling in (d)] during the fingering process with various applied voltage amplitudes. Other parameters were kept constant at droplet volume $V = 3\ \mu$l, viscosity $\nu = 100\ \text{mm}^2/\text{s}$, and gap width $b = 0.1$ mm. The line connecting the maxima in plot (d) is there just to guide the tendency.

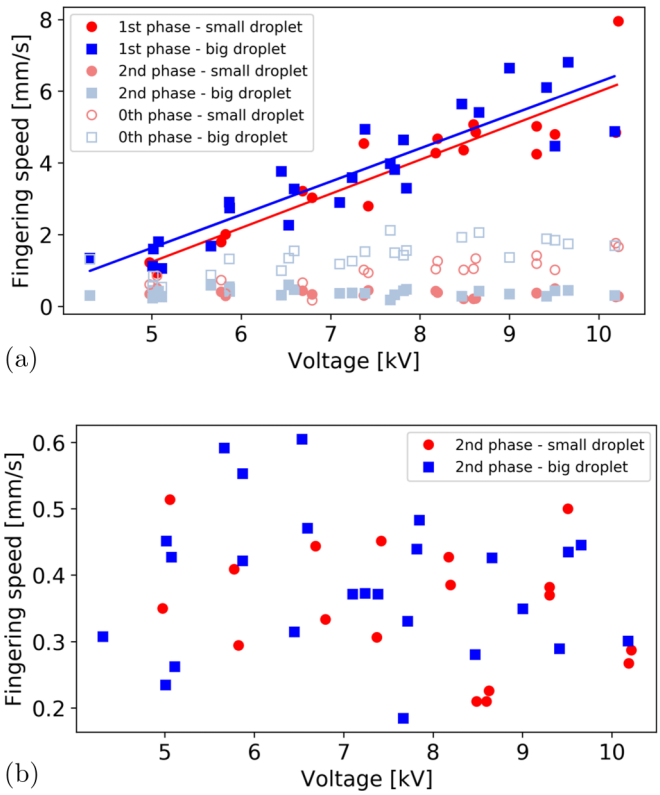

FIG. 14. Dependency of the fingering speed on voltage. The speed was calculated according to Fig. 4(b), separately for each phase of fingering process. (a) The speed of all three phases with emphasis on the first phase. (b) The second phase speed. Experimental conditions: viscosity $\nu = 100$ mm^2/s, gap width $b = 0.1$ mm, small droplet volume $V = 3$ μl, and big droplet volume $V = 8$ μl.

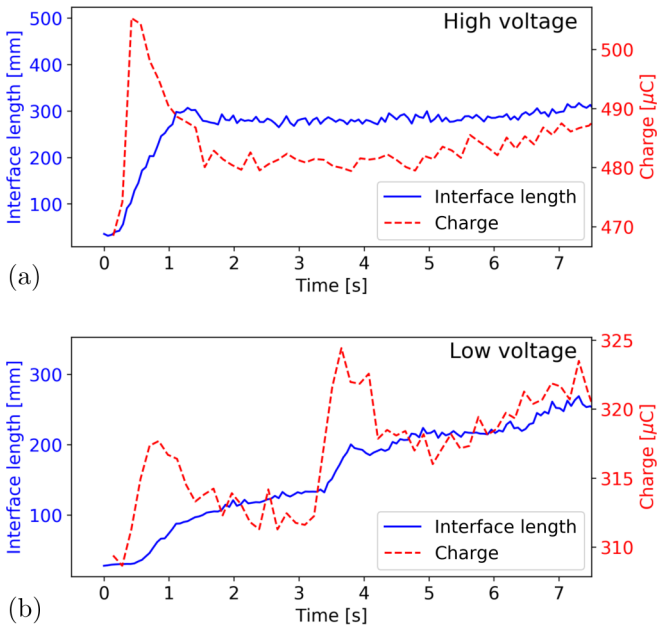

FIG. 15. The comparison of interface length and mean transferred charge trends during fingering process at high (a) and low (b) voltage. Experimental conditions: droplet volume $V = 8$ μl, viscosity $\nu = 100$ mm^2/s, gap width $b = 0.1$ mm, high voltage was $U_{\text{amp}} = 8.4$ kV for (a), and low voltage was $U_{\text{amp}} = 4.5$ kV (b).

shown in zoomed-in detail as a function of the applied voltage amplitude. It is found that there is no apparent dependency between these two parameters. One can conclude that the global applied-voltage parameter does not directly influence the speed of the second phase. But the voltage still affects the intricate fingering, branching and folding phenomena taking place in the second phase as it is clearly observable from the further interface stretching for higher voltages [Fig. 13(a)].

The temporal coincidence in the peaking of the mean transferred charge, and the interface length is obvious from all previously presented figures, see Figs. 4, 9, or 13. Figures 4(c) and 4(d) also reveal that the interface length change reacts to the dissipated power and transferred charge parameter changes. One can conclude that the interface stretching is a direct consequence of the power dissipated in the cell, i.e., of the heat generation which was proposed in Ref. [26]. This fact is well visible also from the comparison of two events with different voltage amplitude, as can be seen in Fig. 15. The dashed red line here is the mean transferred charge (i.e., voltage weighted dissipated power), and the blue solid line is the length of the interface. The first part of the increase of the interface length happens at the same time as an increase in the mean transferred charge, but the rest of interface rapid prolonging is happening while the charge is sharply decreasing. This decrease then stops at certain value [approximately 485 μC for high-voltage event depicted in Fig. 15(a)] and the second phase starts. It can be concluded, that what is essential is not the rising time of transferred charge peak but the duration of the whole peak above some threshold (equilibrial) value. The experimental data for almost half value of the applied voltage amplitude are shown in Fig. 15(b). The charge or interface length peak sequence is even more pronounced, further proving the ties between the two quantities. The delays between the mean transferred charge changes and the interface length changes are longer for lower voltage amplitude experiments ($\sim$0.3 s) than in the high-voltage case ($\sim$0.1 s). It shows that the expansion of the droplet is for lower voltages slower but still the result of the power dissipation in the cell.

To conclude, the discharge activity, as analyzed via time-resolved electrical recording, clearly triggers the change of the interface length. This fact opens a new methodological possibility to analyze such phenomena initiation quantitatively in the future. Later on, in the second phase, the global (spatially unresolved) parameters causality is not clear anymore. We can speculate whether the phenomena become locally driven (i.e., the global parameters become insensitive) or other forces take place in the already too nonlinear phase of the droplet development.

The results of the fractal dimension development for different applied voltages are shown in Fig. 16 together with the development of the accompanied interface length. As already stated above, the uncertainty of the fractal dimension parameter evaluation is in the order of ± 0.03 and therefore the final value (at approx. 5.8 s in this figure) seems to be slightly above 1.8. As expected, the rate of change of the fractal dimension for different voltages is consistent with the rate of change of the interface length. For the highest

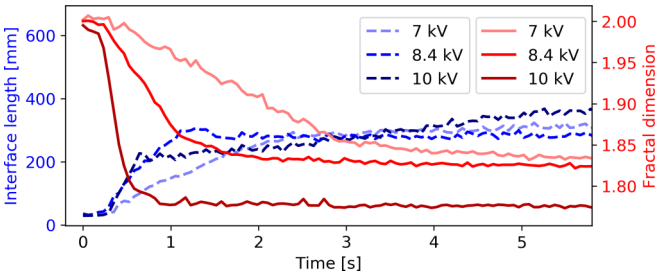

FIG. 16. The comparison of the development of the plasma-liquid interface length (blue dashed lines) and its fractal dimension (red solid lines) for different applied voltage amplitudes. The initial conditions, apart of the applied voltage, were the same: droplet volume $V = 8\ \mu$l, viscosity $\nu = 100$ mm^2/s, and gap width $b = 0.1$ mm.

voltage, the fractal dimension reaches values below 1.8 after at the end of the first phase and almost plateaus around 1.77 value at the sixth second. Such values are given as typical by authors studying the process of normal viscous fingering [43–45] and the similar value was also achieved in the experiment with plasma bubble undergoing fingering process [25]. These values are also interestingly close to the fractal dimension of diffusion-limited aggregation patterns, often stated as 1.71 [45,46].

Finally, the applied voltage parameter strongly influences also the secondary droplets. As the wavelength of fingers decreases with increasing voltage, the thickness of the oil channels separating neighboring fingers decreases as well. The consequence of this can also be seen in the changes of the size of the secondary droplets, as they are formed by tearing off the final part of the oil channels. The results are shown in Fig. 17(a). For various voltages and two different gap widths, the diameters of all secondary droplets found in several frames from ICCD video for each condition were measured. Their average size decreases with the increasing voltage and also with the expanding gap width. For voltages too low, the droplets did not separate from the main oil body and for voltages too high, the droplets became too small to be recognizable in the video. The deviations from average were rather significant, as was expected; the secondary droplets' size is partially dependent also on their traveled distance, as was shown in Fig. 7 and the droplets considered here were captured in different stages of their movement (approximately at the 10th second of the overall process). Figure 17(b) shows the distribution of their sizes for one data point of Fig. 17(a). It should again be noted that the droplets with diameter below 0.1 mm were not recognizable, which probably resulted in asymmetric distribution and a slight shift of average size toward higher values.

V. THEORETICAL ANALYSIS

The theoretical model describing the initial destabilization of the droplet interface based on thermal Marangoni effect induced by the plasma heating was presented by Hou *et al.* [26]. The authors were able to theoretically determine the perturbation wavelength λ_M as a function of the applied voltage, which is directly responsible for the heating effects. The model results in the following formula for determination of the wavelength of the fingering pattern:

$$\lambda_M = \lambda_{\min}\left(\frac{1-\frac{v_{\min}\nu_0\rho_0}{\sigma_0}C\Delta U_{\mathrm{pp}}}{1+C\Delta U_{\mathrm{pp}}}\right)^{1/2}, \tag{5}$$

where the ν_0, ρ_0, and σ_0 denote the viscosity of the fluid, its density and surface tension, respectively, all at temperature $T_0 = 298$ K. The term ΔU_{pp} means the difference between the given peak-to-peak voltage U_{pp} and lowest measured voltage $U_{\mathrm{pp\,min}}$, parameters with lower index "min" are experimentally obtained values of perturbation wavelength $\lambda_{\min}$ and interface velocity $v_{\min}$ measured for the lowest inspected voltage $U_{\mathrm{pp\,min}}$ and C is the coefficient of variation of interface velocity with applied voltage, that needs to be measured as well.

We have followed this approach and results from many events are summarized in the graph in Fig. 18 where all these results form a confidence band (magenta band) for approximately 75% of all obtained data. The black solid line is the simulation using this model for increasing voltage and it serves as a fixed curve relative to the results of many measurements. The range of both axes is relative, as this plot was created as a merge of multiple trends, each for slightly different experimental conditions and in the slightly different data range. Each trend was then plotted using the whole plot window, i.e., with its own twin x and y axes. When plotted in such a way, the simulations for each data set were aligned and the dispersal of experimental data became easily comparable. The minimum and maximum values of lower and upper limits of both axes are displayed in Fig. 18, and it can be seen that

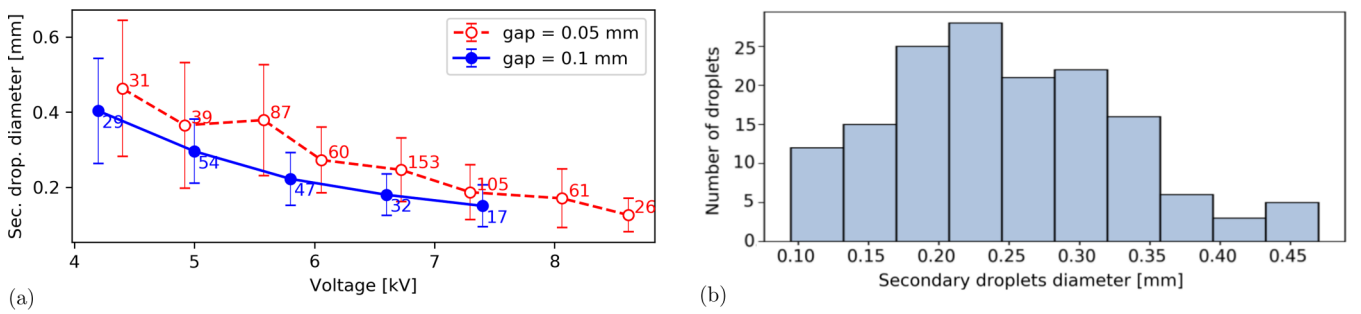

(a) (b)

FIG. 17. (a) The average diameter of secondary droplets for two gap widths and various voltages. The numbers next to the data-points denote the number of secondary droplets used for counting the average. Original droplet was of volume $V = 8\ \mu$l and viscosity $\nu = 100$ mm^2/s. (b) The distribution of secondary droplets sizes for one data point in (a).

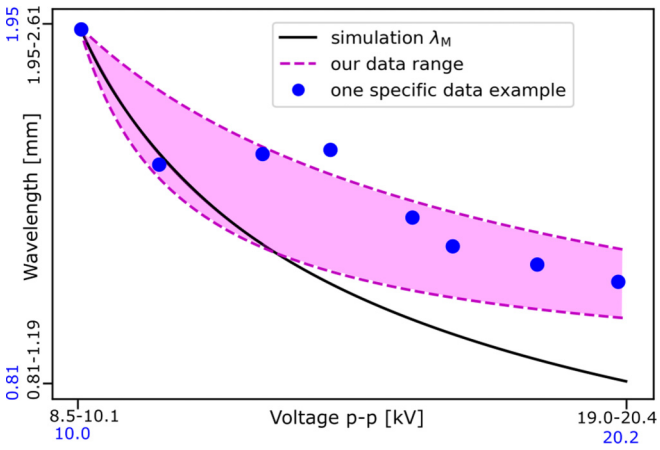

FIG. 18. The comparison of the λ_M simulation based on thermal Marangoni effect model [Eq. (5), black solid line] and our experimental data (magenta area). The plot is a merge of multiple experiments with slightly different voltage ranges and resulting wavelengths, thus the nonstandard presentation of the axes, further explained in the main text. The magenta area represents the 75% confidence band. One of the experimental data set (blue points) is given with relevant scales on both axes (the linear scales are denoted in blue (outer) numbers). The data represent results under following conditions: viscosity $\nu = 100$ mm^2/s, gap width $b = 0.1$ mm and droplet volume $V = 3$ μl (also the blue points) and $V = 8$ μl.

the variation of the ranges is not big. Due to this nonstandard and relative way of plotting, this plot is not intended for any precise quantitative analysis, yet definite qualitative conclusions can be made: It can be seen that the experimental results and the simulation are in agreement mainly for lower voltages. For the lowest voltage, the simulation always fits perfectly, as it directly takes experimental values obtained for this voltage as an input. However, as the voltage increases toward higher values, the model prediction deviates from the experiment increasingly. The values of wavelength for higher voltages become underestimated. A similar result was also observed in Ref. [26], however, the deviation was not so notable there. The experiments in Ref. [26] were only performed for voltages up to 10 kV peak-to-peak (compared to 20 kV peak-to-peak in our experiments).

From our point of view, there is following additional mechanism not yet accounted for in the model, which may be responsible for the observed deviation of the experimental data from the model for higher voltages. It is connected to the change of the viscosity of the fluid due to the increase of the temperature caused by the presence of the discharge. The viscosity of the used silicone oil is a function of temperature:

$$\nu(T) = \nu_0 \exp[B(1/T - 1/T_0)], \tag{6}$$

where ν_0 is viscosity at the temperature $T_0 = 298$ K and $B = 1683$ K (see [47]). This exponential function clearly shows that the viscosity decreases with increasing temperature. The temperature can increase by tens to hundreds of degrees during the several seconds of experiment [39] under given conditions. As a result, the heated layer of the oil in direct contact with the plasma decreases its viscosity and thus its fingering wavelength increases—see the influence of viscosity on the perturbation wavelength in Fig. 10 or in Ref. [26] where the experimental dependence $\lambda \propto b\nu_0^{-1/2}$ is shown. Such an effect is not directly accounted for in the model given by Eq. (5), where the viscosity is taken just for one temperature and the model is not sensitive to its variation. In Eq. (5), the effect of the temperature is treated for surface tension and macroscopic parameter of the fingering velocity, which can be influenced by other effects (e.g., the interface curvature, its stretching or folding). To account for this effect, we have introduced the explicit term

$$A(T) = \sqrt{\frac{\nu(T)_{U_{\mathrm{pp\,min}}}}{\nu(T)_{U_{\mathrm{pp}}}}} \tag{7}$$

into the semiempirical model, so that the new wavelength is defined as

$$\lambda_{M\nu} = \lambda_M A(T), \tag{8}$$

where λ_M is the wavelength calculated with the original model in Ref. [26], see Eq. (5). The term $\nu(T)_{U_{\mathrm{pp\,min}}}$ is the viscosity at minimum used voltage and $\nu(T)_{U_{\mathrm{pp}}}$ is the viscosity at each given voltage. The actual viscosity $\nu(T)_{U_{\mathrm{pp}}}$ was calculated based on the formula in Eq. (6), defining temperature dependence of viscosity. The relation between the temperature in the discharge and voltage is supposed to be linear under given conditions (see Ref. [39]), with fixed coordinate for $T = 298$ K for $U_{\mathrm{pp}} = 0$ kV. We assume that the temperature of the thin interfacial layer corresponds to the discharge temperature. The slope of the line was a fitting parameter, and as a result, we got a different slope for each run. The higher was the experimental data deviation from the original model λ_M (for a given set of data), the steeper was the slope needed to compensate it. The results of this procedure are shown in Fig. 19. Apparently, the viscosity falls by an order of magnitude as the temperature linearly grows.

For easier comprehension of the results, instead of the slope, we describe the effect in terms of the resulting temperature $T_{\max}$ at $U_{\mathrm{pp}} = 20$ kV, which is approximately the maximum voltage used in our experiments. This temperature ranged from 325 K to 507 K for different experiments. It is a reasonable temperature (see also Ref. [39]), as one has to keep in mind that only the thin layer of oil droplet closest to the oil-plasma interface participates in the early fingering process, not the whole bulk of the oil droplet. However, even if the droplet center does not reach as high temperatures as the oil in contact with the plasma, it influences the temperature in the boundary layer through heat conduction. In agreement with this, the highest temperature of 507 K was obtained from the fit for the droplet with smaller volume of 3 μl. Higher volume droplets (8 μl) got heated only to temperatures 325–391 K. The variance in temperatures for individual experiments with the same experimental conditions is still rather high. It was to be expected, considering the deviations in original experimental data were also significant. Nevertheless, the above-performed analyses suggest, that the improved semiempirical model could also be used as a thermal probe under given conditions.

The effect of the changing viscosity with temperature however, does not have to be the only other mechanism affecting the perturbation wavelength. In the Hele-Shaw cell

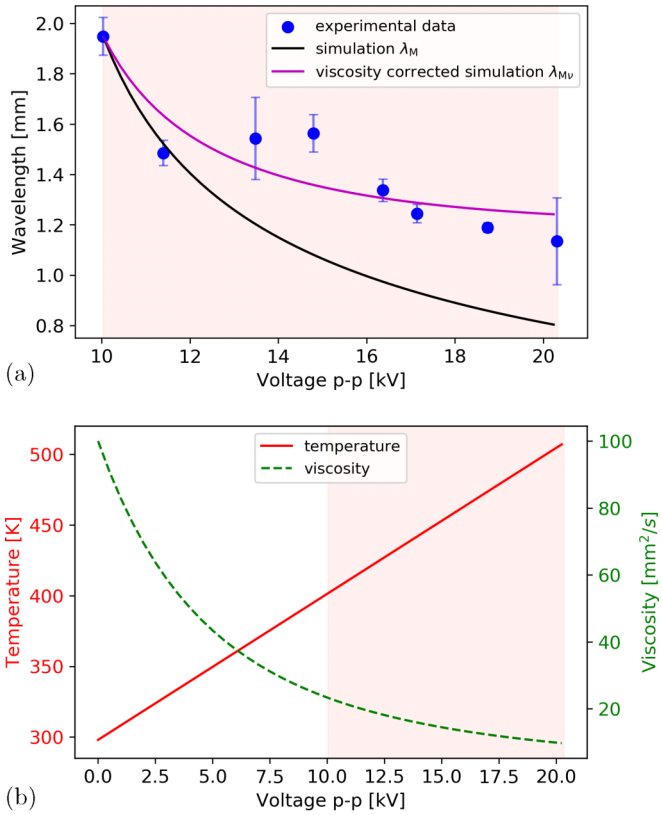

FIG. 19. In the part (a), the experimental data (conditions as in Fig. 18) with simulations for λ_M [Eq. (5)] and for improved model for $\lambda_{M\nu}$ [Eq. (8)] with thermally sensitive viscosity $\nu(T)$ given by multiplication factor from Eq. (7) are shown. In part (b), the corresponding temperature and viscosity variations with the applied voltage are shown as a result from the fitting procedure.

with perpendicular electric fields, the electrostatic pressure could also be affecting the droplet in a way not included in the model. For such an analysis, the gap voltage is one of the critical parameters. As mentioned above, the applied voltage measured in the external circuit is not describing the electrical conditions in the Hele-Shaw cell accurately. We intend to explore these effects in the future.

VI. SUMMARY AND CONCLUSION

This paper presented detailed experimentally obtained results of dynamic phenomena accompanying the interactions of nonconductive oil droplet and dielectric barrier discharge plasma. The process of plasma and liquid oil interaction was mapped throughout its whole lifespan, from an initial periodic perturbation, through an abrupt and fast expansion of the droplet forming thin oil channels, their stretching and folding, until the final state of the droplet fragmentation into tens of tiny secondary droplets, fundamental units of fingering instability too small to split any further. The shape and movement of the oil-plasma interface was characterized in terms of the perturbation wavelength, speed of the fingering process, the total length of the plasma-liquid interface and its fractal dimension. The detailed time-resolved optical recordings enabled not only a unique quantified picture of the whole phenomenon but also a useful large amount of experimental data available for direct comparison with possible future computer simulations.

The electrical measurements synchronized with optical monitoring provided us with temporal recordings of mean dissipated power in the system, and its voltage-weighted analogy of the mean transferred charge. These parameters development showed a remarkable correlation with the stretching of the interface length, clearly identifying the high power dissipation in the system as the cause of the instability initiation and further interface stretching. These findings allow using the developed electrical-based methodology for more detailed investigation of destabilization-driving forces in the future characterization of such phenomena.

Moreover, the results of our parametric study showed that the viscosity of the oil and the discharge voltage had a profound impact on the experiment, affecting not only the wavelength of the perturbation and resulting pattern, but also the timing and the speed of the fingering process evaluated quantitatively via parameters mentioned above. The parametric study for fingering events at higher voltages revealed a systematic inconsistency with know model describing the destabilization based on thermal Marangoni effect. Taking into account the contribution of the changing viscosity with temperature, we propose an explanation of the observed inconsistency and identify the previously neglected effect which has to be taken into account additionally. The developed model opens new possibilities for temperature estimation of the destabilized liquid interface.

Thanks to the parametric mapping of the complete process of the droplet-plasma interactions, and combining temporally resolved and synchronized visual and electrical data, we were able to present time-dependent description of the fingering instability at the plasma-liquid interface and enhance its theoretical analysis. We believe that both, the analyzed system and newly developed methods, give an opportunity for the further more-profound study of the plasma-liquid interface, which is of high importance for the broader low-temperature plasma community.

ACKNOWLEDGMENTS

This research has been supported by Project No. LM2018097 funded by Ministry of Education, Youth and Sports of the Czech Republic.

[1] G. I. Taylor, Proc. Roy. Soc. A: Math. Phys. **201**, 192 (1950).
[2] L. Rayleigh, Sci. Papers, 200 (1900).
[3] H. Kull, Phys. Rep. **206**, 197 (1991).
[4] W. Thomson, Lond. Edinb. Dubl. Philos. Mag. J. Sci. **42**, 362 (1871).
[5] H. von Helmholtz, *über discontinuirliche Flüssigkeits-Bewegungen* (Akademie der Wissenschaften zu Berlin, 1868).

[6] P. G. Saffman and G. I. Taylor, P. Roy. Soc. A: Math. Phys. **245**, 312 (1958).
[7] R. Chuoke, P. Van Meurs, and C. van der Poel, Petrol. Trans. **216**, 188 (1959).
[8] S. Hill *et al.*, Chem. Eng. Sci. **1**, 247 (1952).
[9] J. Zeleny, Phys. Rev. **10**, 1 (1917).
[10] G. I. Taylor, P. Roy. Soc. A: Math. Phys. **280**, 383 (1964).
[11] F. E. Ahmed, B. S. Lalia, and R. Hashaikeh, Desalination **356**, 15 (2015).
[12] A. Jaworek and A. T. Sobczyk, J. Electrostat. **66**, 197 (2008).
[13] Q. Wang and D. Papageorgiou, J. Fluid Mech. **683**, 27 (2011).
[14] A. A. Fragkopoulos, A. Aizenman, and A. Fernández-Nieves, Phys. Rev. Lett. **118**, 264501 (2017).
[15] P. Rumbach, D. M. Bartels, R. M. Sankaran, and D. B. Go, Nat. Commun. **6**, 7248 (2015).
[16] P. J. Bruggeman, M. J. Kushner, B. R. Locke *et al.*, Plasma Sources Sci. Technol. **25**, 053002 (2016).
[17] P. Rumbach, J. P. Clarke, and D. B. Go, Phys. Rev. E **95**, 053203 (2017).
[18] P. Vanraes and A. Bogaerts, Appl. Phys. Rev. **5**, 031103 (2018).
[19] M. Šimek, B. Pongrác, V. Babický, M. Člupek, and P. Lukeš, Plasma Sources Sci. Technol. **26**, 07LT01 (2017).
[20] R. Banaschik, P. Lukes, C. Miron, R. Banaschik, A. V. Pipa, K. Fricke, P. J. Bednarski, and J. F. Kolb, Electrochim. Acta **245**, 539 (2017).
[21] J. Kang, O. L. Li, and N. Saito, Carbon **60**, 292 (2013).
[22] K. Tachibana, Y. Takekata, Y. Mizumoto, H. Motomura, and M. Jinno, Plasma Sources Sci. Technol. **20**, 034005 (2011).
[23] J. F. M. van Rens, J. T. Schoof, F. C. Ummelen, D. C. van Vugt, P. J. Bruggeman, and E. M. van Veldhuizen, IEEE Plasma Sci. **42**, 2622 (2014).
[24] B. S. Sommers, J. E. Foster, N. Y. Babaeva, and M. J. Kushner, J. Phys. D **44**, 082001 (2011).
[25] H.-Y. Chu and H.-K. Lee, Phys. Rev. Lett. **107**, 225001 (2011).
[26] S.-Y. Hou and H.-Y. Chu, Phys. Rev. E **92**, 013101 (2015).
[27] T. E. Oliphant, *A Guide to NumPy*, Vol. 1 (Trelgol, USA, 2006).
[28] G. Bradski, Dr. Dobb's Journal of Software Tools (2000).
[29] J. Canny, IEEE Trans. Pattern Anal. Mach. Intell. **PAMI-8**, 679 (1986).
[30] R. Brandenburg, Plasma Sources Sci. Technol. **26**, 053001 (2017).
[31] B. Pashaia, R. Sankaranarayanan, and S. K. Dhali, IEEE Plasma Sci. **27**, 22 (1999).
[32] J. Ráheľ and D. M. Sherman, J. Phys. D **38**, 547 (2005).
[33] Z. Fang, J. Lin, X. Xie, Y. Qiu, and E. Kuffel, J. Phys. D **42**, 085203 (2009).
[34] L. Stollenwerk, S. Amiranashvili, J.-P. Boeuf, and H.-G. Purwins, Phys. Rev. Lett. **96**, 255001 (2006).
[35] L. Dong, W. Fan, Y. He, and F. Liu, IEEE Plasma Sci. **36**, 1356 (2008).
[36] See Supplemental Material at http://link.aps.org/supplemental/10.1103/PhysRevE.101.063201 for exemplary evolution of the oil droplet affected by plasma.
[37] J. Theiler, J. Opt. Soc. Am. A **7**, 1055 (1990).
[38] F. J. J. Peeters and M. C. M. van de Sanden, Plasma Sources Sci. Technol. **24**, 015016 (2014).
[39] N. Naudé, J.-P. Cambronne, N. Gherardi, and F. Massines, J. Phys. D **38**, 530 (2005).
[40] J. C. Vassilicos and J. C. R. Hunt, Proc. Roy. Soc. A: Math. Phys. Sci. **435**, 505 (1991).
[41] G. M. Homsy, Ann. Rev. Fluid Mech. **19**, 271 (1987).
[42] L. Paterson, J. Fluid Mech. **113**, 513 (1981).
[43] S. E. May and J. V. Maher, Phys. Rev. A **40**, 1723(R) (1989).
[44] J.-D. Chen, J. Fluid Mech. **201**, 223 (1989).
[45] O. Praud and H. L. Swinney, Phys. Rev. E **72**, 011406 (2005).
[46] G. Daccord, J. Nittmann, and H. E. Stanley, Phys. Rev. Lett. **56**, 336 (1986).
[47] *Bluesil FLD 47 Technical Information* (Bluestar Silicones, 2014).